

# Studying the performance and accuracy of PFEM-2 in the solution of biomedical benchmarks

Facundo Del Pin · Chien-Jung Huang  
Iñaki Caldichoury · Rodrigo R. Paz

February 4, 2019

**Abstract** In recent years the biomedical industry has shown increased interest in using numerical methods to assist in the R&D of medical devices. The long term goal is to reduce the costly and lengthy process that clinical trials take to for the US Food and Drug Administration (FDA) to approve a medical device. For this reason both FDA and academia are working together to create laboratory experiment that will help the industry gain confidence in numerical techniques as well as provide software developers with insights on the deficiencies and strength that numerical software may have. In this article three benchmarks proposed by the FDA are used to compare experimental results with those of the Finite Element Method (FEM) and Enhanced Particle Finite Element Method (PFEM-2). The first benchmark problem is the flow in a nozzle containing a gradual and sudden change of diameter with the goal of predicting hemolysis (not studied in this work). The second problem studies the flow in a simplified centrifugal blood pump under various pump operation conditions. Finally the third benchmark studies the steady flow in a patient-averaged inferior vena cava. PFEM-2 is regarded as a tool with great potential mainly because no stabilization is needed for the Galerkin approximation of the advection term in the transport equations. This could be a big advantage in problems with flows at high Reynolds number. The improved integration along streamlines provide a more accurate way to analyze problem with large time step.

This paper is an effort to test PFEM-2 in real world engineering applications.

**Keywords** Particle Method · Finite Element · Biomedical Devices · CFD · Benchmarks · FDA

## 1 Introduction

A key step in the development of medical devices is the testing phase. Regulatory agencies like the Food and Drug Administration (FDA) require extensive laboratory testing and a long, tedious and expensive clinical trial process before a device is approved for clinical use. In an effort to optimize this process the industry and the regulatory agencies are looking at numerical methods as an additional tool that could potentially reduce the time of product development, animal testing and cost. A first critical step to do this end is to increase the confidence, reliability and robustness of numerical techniques. The FDA is actively working on this subject by designing laboratory experiments that could be used to evaluate the solution accuracy provided by computational methods launching the Critical Path Initiative (CPI) [2] program. The aim of the program is to standardize the use of computational simulation on the design of the blood-contacting medical devices and analysis of the ratio of hemolysis in them. The goal of this project is to establish the guidelines for applying CFD on the evaluation and the optimization of the medical devices. FDA has proposed two benchmark problems [1] for CFD verification and validation. The first benchmark problem is the flow in a nozzle containing a gradual and sudden change of the diameter. The flows at different flow rates which correspond to different flow regimes are examined. The second study is the flow in a simplified centrifugal blood pump. The flow

---

Livermore Software Technology Corporation  
Livermore, CA, United States  
E-mail: fdelpin@lstc.com  
E-mail: cjhuang@lstc.com  
E-mail: inaki@lstc.com  
E-mail: rpaz@lstc.com

field under various pump operation conditions are analyzed. For each benchmark problem, the experimental results [3–5] and the flow field predicted with numerical simulations [6–9] from different institutes are collected. The comparison between results obtained using different numerical models are made and analyzed [10, 11].

Additionally a third benchmark problem will be presented which involves the analysis of steady flow in a patient-averaged inferior vena cava [12, 13]. Although there are many numerical results in this area only a few compare with flow measurements of experimental results. In particular the study represents an anatomical model of the inferior vena cava (IVC) that includes the primary morphological features that influence the hemodynamics (iliac veins, infrarenal curvature, and non-circular vessel cross-section).

In this study, these three benchmark problems will be presented and contrasted with numerical results using the Finite Element Method (FEM) and the enhanced Particle Finite Element Method (PFEM-2).

The main goal of this paper is to evaluate the performance of the PFEM2 method in the field of biomedical devices comparing the predictions with the experimental results. The PFEM2 method is based on the idea that advection effects are approximated in a Lagrangian way using particles. Many numerical methods are based on these ideas [14–18] including the early version of PFEM [19]. In the latter the advection and all derivatives were computed on a finite element mesh that had to be re-constructed at every time step due to the Lagrangian nature of the method. All the fields were approximated using the FEM. The PFEM provides excellent results in problems with free surface or fluid structure interaction but it had poor performance in problems involving internal/external aerodynamics when compared to Eulerian methods due to the additional mesh operations which in turn also force a complete re-factorization of all linear systems. The work of Idelsohn et. al. [20, 21] introduced a new integration strategy called X-IVS that employed a fixed mesh modifying the PFEM and creating PFEM-2. Not only these improvements made PFEM-2 competitive in problems classically solved using Eulerian methods but it provided the advantage that larger time steps could be used [22] reducing the computational time in advection dominated problems and eliminating the traditional advection stabilization terms known to introduce additional numerical diffusion. By eliminating the advection term a fractional step method provides a fully decoupled momentum equation among the three velocity components which saves storage and simplify the implementation. The left hand side also becomes symmetric allowing the use of simpler linear algebra solvers like

Conjugate Gradient [23]. The method has also been successfully implemented for multi-phase flows [24, 25, 28], problems involving surface tension [27] and fluid structure interaction [26].

There are many applications in the biomedical field that could benefit from the capabilities of PFEM-2. In particular those applications that involve long real time simulations like drug delivery where a fluid component is injected in another fluid. In this case it is also important to keep track of the sharp interface at the drug advancing front. **MORE APPLICATIONS**

In this work the implementation of PFEM-2 was performed in the commercial software LS-DYNA® which is a multi-physics solver for non-linear dynamics. The module used for the implementation was ICFD which deals with incompressible fluid flows.

The rest of this paper will be organized as follows. In the first section the equations governing the flow of incompressible fluids will be presented together with boundary and initial conditions. In section two the PFEM-2 method will be introduced and some implementation aspects will be discussed. In section three the time and space discretization of the equations of motion will be presented. In section four the benchmark problems will be introduced and the experimental and numerical results will be presented.

## 2 Equations of Motion

The benchmarks presented in this article study the motion of incompressible flows and their interaction with rigid solid boundaries. In this case the equations of motion for the continuous model are defined by the Navier-Stokes equations and the continuity equation. Let  $\Omega \subset \mathbb{R}^n$  be the spatial domain at time  $t \in [0, T]$  with  $n$  the number of space dimensions then the system of equations is defined by:

$$\rho D_t \mathbf{u} - \nabla \cdot \boldsymbol{\sigma} = \mathbf{f} \text{ in } \Omega \times [0, T] \quad (1)$$

$$\nabla \cdot \mathbf{u} = 0 \text{ in } \Omega \times [0, T] \quad (2)$$

where  $\rho$  is the fluid density and  $\mathbf{u}$  is the velocity,  $\mathbf{f}$  is the body force and  $\boldsymbol{\sigma}$  is the stress tensor:

$$\boldsymbol{\sigma} = 2\mu\boldsymbol{\epsilon}(\mathbf{u}) - p\mathbf{I} \quad (3)$$

with  $p$  the fluid pressure,  $\mu$  the dynamic viscosity and  $\mathbf{I}$  the identity tensor and  $\boldsymbol{\epsilon}$  the strain-rate tensor defined as:

$$\boldsymbol{\epsilon}(\mathbf{u}) = \frac{1}{2}(\nabla \mathbf{u} + \nabla \mathbf{u}^t) \quad (4)$$

Eq. (1) needs Dirichlet and Neuman boundary conditions expressed as:

$$\mathbf{u} = \mathbf{g} \text{ on } \Gamma_g \times [0, T] \quad (5)$$

$$\mathbf{n} \cdot \boldsymbol{\sigma} = \mathbf{h} \text{ on } \Gamma_h \times [0, T] \quad (6)$$

where  $\Gamma_g$  and  $\Gamma_h$  are complementary subsets of the domain boundary  $\Gamma$ . The functions  $\mathbf{g}$  and  $\mathbf{h}$  are both given and  $\mathbf{n}$  is the unit normal vector pointing outward from the domain. The initial condition is specified on the domain  $\Omega$  at  $t = 0$ :

$$\mathbf{u}(\mathbf{x}, 0) = \mathbf{u}_0(\mathbf{x}) \quad (7)$$

where  $\mathbf{u}_0(\mathbf{x})$  is a divergence free velocity field.

The expression of Eq. (1) was written using a material derivative since this paper will deal with both a Lagrangian and a Eulerian formulation. In the case of an Eulerian framework the material derivative becomes:

$$D_t \mathbf{u} = \partial_t \mathbf{u} + \mathbf{u} \cdot \nabla \mathbf{u} \quad (8)$$

It is important to note that the last term on the right hand side is non-linear with respect to the fluid velocity  $\mathbf{u}$ .

### 3 Numerical Method

The numerical scheme used in the approximation of the system of Eq. (1-2) is based on FEM. The Galerkin method will be used with a  $p_1 - p_1$  interpolation space for the pressure-velocity pair. Furthermore the discrete model will be decoupled by means of a fractional step method first proposed by Chorin [31] and Temam [32]. To simplify the presentation a backward difference time integration scheme was used for the time derivative of  $\mathbf{u}$  but another higher order scheme may also be used.

$$\rho(\mathbf{M}\mathbf{u}^* - \mathbf{M}\hat{\mathbf{u}}^n)/\Delta t + \mu\mathbf{K}\mathbf{u}^* + \beta\rho\mathbf{S}(\bar{\mathbf{u}}^{n+1})\mathbf{u}^* = -\mathbf{G}\mathbf{p}^n + \mathbf{F}, \quad (9)$$

$$\mathbf{L}\mathbf{p}^{n+1} = \frac{\rho}{\Delta t}\mathbf{D}\mathbf{u}^* + \mathbf{L}\mathbf{p}^n, \quad (10)$$

$$\rho\bar{\mathbf{M}}\mathbf{u}^{n+1} = \rho\bar{\mathbf{M}}\mathbf{u}^* - \Delta t\mathbf{G}(\mathbf{p}^{n+1} - \mathbf{p}^n), \quad (11)$$

where the standard assembled FEM matrices are  $\mathbf{M}$  for the mass matrix,  $\mathbf{K}$  is the stiffness matrix,  $\mathbf{L}$  is the Laplacian matrix,  $\mathbf{D}$  is the divergence,  $\mathbf{G}$  is the gradient matrix and  $\bar{\mathbf{M}}$  is the lumped mass matrix. The vector  $\mathbf{F}$  is the body force term. The matrix  $\mathbf{S}$  is the advection matrix which depends on the fluid velocity. The switch  $\beta$  will define whether the advection is done in a Eulerian way or Lagrangian by using PFEM-2. The variable  $\mathbf{u}^*$  is an intermediate velocity that is predicted using the pressure from  $t^n$ . As such it is not yet divergence free and it has to be corrected in the last step. When  $\beta = 1$  the advection term is used to transport the velocity and then it takes the value  $\hat{\mathbf{u}}^n = \mathbf{u}^n$  which is the velocity from the previous time step  $t^n$ . When  $\beta = 0$  the particles transport the velocity which has to be projected back onto the mesh nodes. More about this projection will be discussed later.

In this work standard  $p_1 - p_1$  elements are implemented which do not satisfy the Babuzka-Brezzi condition and thus pressure stabilization needs to be added. Although the fractional step methos adds sufficient numerical compressibility to make stable when time steps are relatively large the second order version of the method loses this property. In this work the Orthogonal Subgrid-Scale (OSS) method by Codina [30] was implemented to prevent this problem. In a similar fashion the Galerkin approximation of the advection terms need to be stabilized for the FEM approximation only case. Again the ideas of Codina as described in [29] are implemented and the OSS method is used.

### 3.1 The PFEM-2 method

The PFEM-2 method is a generalization of the Particle Finite Element Method (PFEM) [19] where the particles are not restricted to the mesh nodes. Massless particles are added everywhere in the mesh and the advection is done by transporting the particles. The main benefit is that now the nodes of the mesh do not have to be moved as was the case in [19] saving many remeshing operations while maintaining the Lagrangian advection. In [20] Idelsohn et. al. present an integration scheme called *Explicit Integration following the Velocity Streamlines* (X-IVS) which is used to integrate the trajectory of particles in PFEM-2. Using this technique the position of a particle  $p$  at time  $t^{n+1}$  ( $\mathbf{x}_p^{n+1}$ ) is computed using the velocity streamlines at  $t^n$ :

$$\begin{cases} \mathbf{x}_p^{n+1} = \mathbf{x}_p^n + \int_n^{n+1} \mathbf{u}^n(\mathbf{x}_p^\tau) d\tau \\ \hat{\mathbf{u}}_p^{n+1} = \mathbf{u}_p^n \end{cases} \quad (12)$$

The expression in Eq. 12 is explicit since it only depends on values from time step  $t^n$  while it maintains the high order approximation used for the velocity field. This expression is not an exact integration since the integral is evaluated following a pseudo-trajectory of the particles calculated with the velocity streamlines within each time step instead of following the true trajectory. Eq. 12 may be integrated analytically or using any standard time integration scheme like explicit Runge-Kutta or using sub-stepping. This new integration proposal provides an efficient strategy to employ time-steps which allow a Courant-Friedrich-Levy (CFL) number larger than one, where:

$$CFL = \frac{|\mathbf{u}| \Delta t}{\Delta x} \quad (13)$$

In summary this means that each particle will be able to travel more than one element without compromising the stability of the method.

It is important to remark that the particles carry valuable information from all the states previous to their current location and preserving that information will have a big influence in the final accuracy of the method. That is why instead of interpolating the mesh velocity to the particle the change of the mesh velocity should be applied. So in Eq. 12:

$$\mathbf{u}_p^n = \mathbf{u}_p^{n-1} + \sum_i N_i(\mathbf{x}_p^n) (\mathbf{u}_i^n - \mathbf{u}_i^{n-1}). \quad (14)$$

being  $N$  the shape function of node  $i$  for the host element of particle  $p$ . In Fig. 1 the trajectory of a particle is

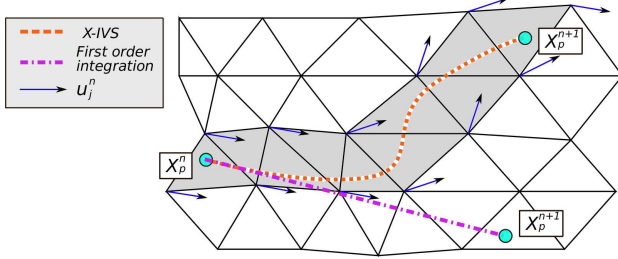


**Fig. 1** Comparison of the trajectory of a particle moving from  $x_p^n$  to  $x_p^{n+1}$  for a given  $\Delta t$  using the X-IVS method and a first order integration scheme for a  $CFL >> 1$ .

computed using the X-IVS method and it is compared to the trajectory of a first order integration scheme for a  $CFL >> 1$ .

Once the particles are moved to their new  $t^{n+1}$  position the field  $\phi$  that they transport (velocity, temperature, level set, etc.) needs to be mapped back to the mesh to perform the FEM analysis. Several approaches have been presented in [28]. In the current work the Global Least Squares Consistent (GLSC) methodology has been implemented and applied to our test cases. This approach solves a minimization problem where the approximation functions are the same linear shape functions used by the FEM discretization. This results in a global system where the unknowns are the nodal values. The minimization problem will be solved for  $\phi$  such that it minimizes a global error function  $E_g$  which computes the quadratic difference between the particle states  $\phi_p$  at positions  $\mathbf{x}_p$  surrounding a node at position  $\mathbf{x}_j$  and the nodal value  $\phi_j$ :

$$E_g(\phi_1, \phi_2, \dots, \phi_j) = \frac{1}{2} \sum_{p=1}^P \left( \phi_p - \sum_{j=1}^J \phi_j N_j(\mathbf{x}_p) \right)^2. \quad (15)$$

To minimize  $E_g$  equation 15 is derived with respect to  $\phi_j$  and equaled to zero leading to the system of  $J$  unknowns:

$$\mathbf{M}\phi = \mathbf{f} \quad (16)$$

where  $J$  is the total number of nodes in the mesh,  $\mathbf{M}_{ij} = \sum_p N_i(\mathbf{x}_p) N_j(\mathbf{x}_p)$  is a consistent mass matrix,  $\phi$  are the unknown nodal values and  $\mathbf{f}_i = \sum_p N_i(\mathbf{x}_p) \phi_p$ .

A step by step summary of the final algorithm for solving Navier-Stokes using fractional step and PFEM-2 is explained in Algorithm 1.

**Algorithm 1** Summary of the steps needed for solving Navier-Stokes using fractional steps and PFEM-2.

- 1: Compute the convection moving particles along streamlines (X-IVS)(Eq. 12).
- 2: Map particle velocities to mesh (Eq. 16).
- 3: Solve the system of Eq. 9-11 with  $\beta = 0$ .
- 4: Correct velocity on particles (Eq. 14).
- 5: Reseed particles if necessary.
- 6: Remove particles if allowed.

Another aspect of PFEM-2 which is more widely discussed in [36] is that of particle inventory. Essentially is the question of when, where and how to add or remove particles. In the present implementation particles are seeded into all the elements at initialization. There is a constant amount of particles per element at the beginning of a run. The number of initial particles can change for different problems. In this work all elements are seeded with twelve initial particles in  $3-d$  and nine in  $2-d$ . Since the objective of this paper is to evaluate the accuracy of PFEM-2 and compare it to that of FEM and experimental results then no strategy has been used to remove particles for the results presented later. The idea is to use PFEM-2 to its full accuracy capacity and removing particles is associated to a loss of accuracy by introducing numerical diffusion. Particles are added to the simulation to maintain a minimum amount of particles per element. This is a difference compared to [36] where the metric used to add particles is associated to the node. This will obviously decrease the computational performance of the simulation since the amount of particles will increase. The implementation relies on a robust parallel implementation to account for the increased demand of memory and CPU due to the increased number of particles. More on this subject will be explained in the next section. As an example to illustrate this issue a simple problem considering the flow past a  $2-d$  cylinder is used (see Fig. 2). It is better to use a  $2-d$  model for illustrative purposes. In Fig. 3 the initial configuration “A” is compared to an advanced configuration “B”. Initially all elements have the same amount of particles and the distribution is homogeneous. As the flow evolves particles agglomerate increasing the overall amount of particles in the domain. Finally figure 4 shows a curve with the number of particles as a function of time. Note how

the number of particles increase rapidly at the beginning of the simulation and then reaches a pseudo-steady state amount. The objective of future implementations will be to attempt to maintain a constant number of particles while preserving the accuracy of the method. There is more about the particle inventory implications for parallel implementations in the next section.

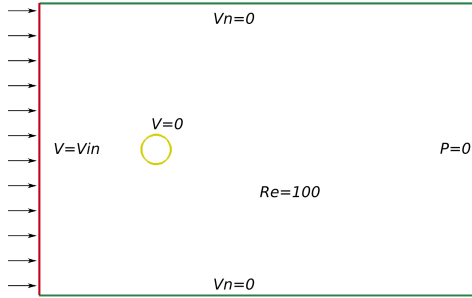


**Fig. 2** Problem definition for the  $2-d$  cylinder problem and boundary conditions.

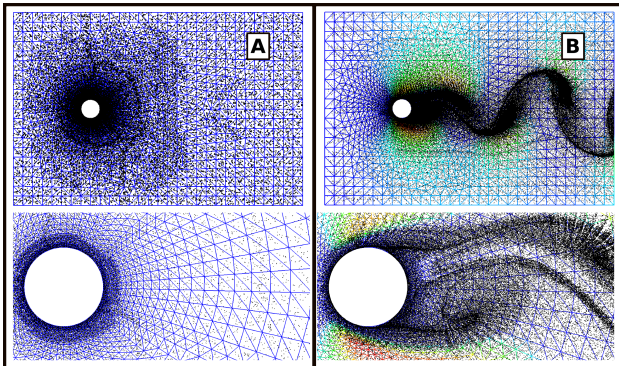


**Fig. 3** Evolution of particle position and number of particles for the  $2-d$  cylinder problem. A) Initial configuration and B) advanced particle configuration.

### 3.2 Parallel Implementation

The parallel implementation for PFEM-2 follows the guidelines presented in [22] for the case of distributed memory architectures. The challenges of serial implementations are well described in their paper but basically involves the extra amount of memory needed for the particle data structure. Due to the explicit scheme the parallel implementation needs to take care of local operations for each particle separately from the rest allowing for a relatively simple parallelization. The difficulty arise at the interface between processors where particles may travel several elements and possible processors before finding their final host element. This task

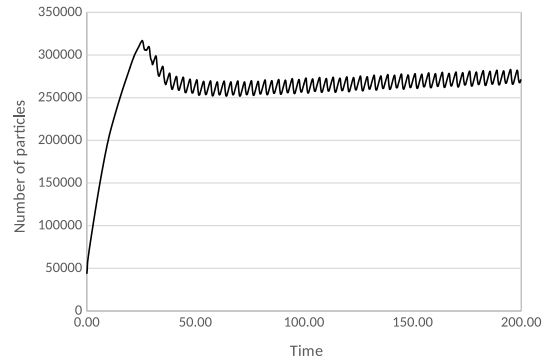


**Fig. 4** Number of particles as a function of a non-dimensional time for the cylinder problem. Observe how the particle number increase rapidly and then they reach a pseudo-steady state amount.

requires an outer loop to communicate particles among processors. This loop will terminate when no more particles cross the interface between partitions. In Fig. 5 there is an illustration of how particles may move across processors. The thick black line depicts the partition. In the first case a particle lands in the same processor which involves no communication. In the second case a particle moves across a single interface and communication takes place. In the third place a particle may move across two or more processors in which case the outer loop will perform as many communications as necessary until no more particles cross a processor interface. The

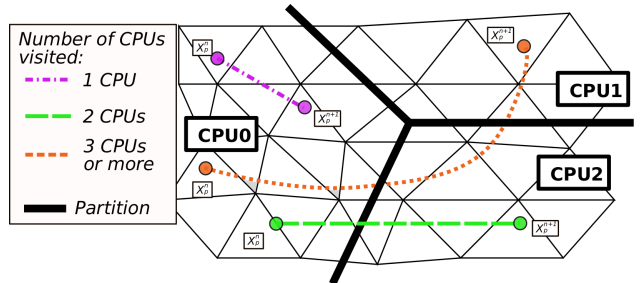


**Fig. 5** Different ways that particles may move across processor interfaces.

current approach is built “on top” of a pre-existing parallel FEM implementation thus inheriting much of the data structures and methodologies where the partitions are created using the software METIS [34, 35].

In the present implementation load balancing has not being addressed. Strictly speaking if particles are not removed from the domain then accumulation of particles in one partition will be an issue. As mentioned before the idea of this paper is to evaluate PFEM-2 without introducing the error associated to the removal of

particles. A future implementation will tackle this issue. The techniques for particle inventory presented in [36] will be a good starting point for the implementation.

To exemplify scalability a  $3-d$  problem of the flow past a cylinder is used. It has a relatively small number of elements of about 200K compared to the element numbers used in the application examples. In figure 6 the strong scalability of the full formulation (FEM+PFEM-2) is shown for distributed memory parallelization. There are two curves for two different inventory strategies. To show the advantages and importance of implementing a particle inventory strategy that is able to remove particles in the first case the number of particles is kept constant at each element regardless of the accuracy of the result. The total number of particles in this case is around 5.7M. In the second case the number of particles changes. No particle is removed from the model except for those that leave the domain and particles are added in elements with less than 12 particles. So the total number of particles is expected to increase as shown in Fig. 4. The final number reaches about 30M particles. Since there is no load balancing particles that accumulate in an element are expected to degrade the scalability which is what is observed in 6. The total scalability for the first case compares well with that of [22].

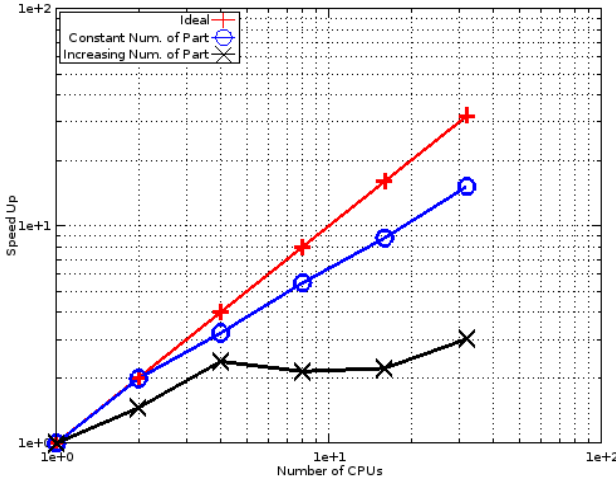


**Fig. 6** Comparison of scalability plots for the cases where the number of particles per element is kept constant and the case where no particle removal takes place so the number of particles increase without load balancing.

#### 4 Numerical results

The simulations of blood flows in nozzle, pump, and IVC with FEM and PFEM-2 are conducted and com-

pared with experimental results in [3], [4], [5] and [12]. The fluid is assumed to be Newtonian blood analog fluid. For the nozzle and pump flows, the fluid density and viscosity are  $\rho = 1035 \text{ kg/m}^3$  and  $\mu = 3.5 \times 10^{-3} \text{ N-s/m}^2$ , where as for the flow in IVC, the density and viscosity are  $\rho = 1817 \text{ kg/m}^3$ ,  $\mu = 5.83 \times 10^{-3} \text{ N-s/m}^2$  for resting condition and  $\mu = 5.49 \times 10^{-3} \text{ N-s/m}^2$  for exercising condition.

#### 4.1 Blood Nozzle

The simplified nozzle proposed by FDA consists of four parts containing characteristics of some blood-conveying medical devices. There are inlet and outlet tubes with diameter 0.012 m, as well as a cone-shaped converging tube connecting the inlet tube with the nozzle throat with diameter 0.004 m as shown in figure 7. The flow experiences a gradual contraction of area from the inlet tube to the throat, then a sudden expansion of the area right after the throat to the outlet tube (figure 8). It is set that the z coordinate along the axial direction has origin at the exit of the nozzle throat. The flow with Reynolds number 3500 with flowrate  $3.64 \times 10^{-5} \text{ m}^3/\text{s}$  corresponding to turbulent flow regime is analyzed, where the Reynolds number is defined with the flow rate and the diameter at the throat.

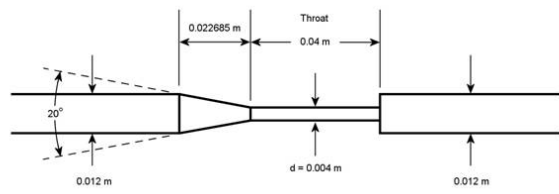


**Fig. 7** The dimension of the idealized nozzle model proposed by FDA.

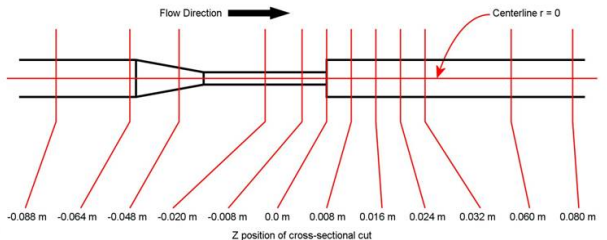


**Fig. 8** The flow direction and the definition of the axial coordinate z.

For the set up of the numerical simulation, the simulation domain starts from  $z = -0.18 \text{ m}$  to  $z = 0.18 \text{ m}$ .

The prescribed uniformly distributed velocity profile is imposed at the inlet while the pressure is constant at outlet. The Large Eddy Simulation (LES) Smagorinsky model is chosen to deal with the turbulent flow regime in nozzle, and the Smagorinsky coefficient is set to be 0.1 empirically for flows in the pipe. The turbulence intensity is set to be 5% at the inlet. There are two different kinds of meshes considered in this study: mesh A with a more uniform mesh size in the outlet tube, and mesh B has a more refined mesh at certain area (figure 9). The mesh A has minimum mesh size 0.2 mm and a total of 8.61M elements. The mesh B has coarser meshes in the outlet tube than mesh A, but has mesh refinement near the exit of the throat. The minimum mesh size of mesh B is 0.1 mm with total of 1.13M elements. The purpose of using two distinct meshes is to observe the influence of mesh on FEM and PFEM-2. [??] Simulations with different CFL number will also be done to examine the influence of time step size with these two methods.

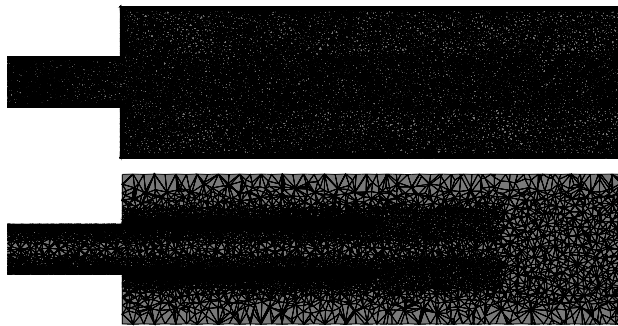


**Fig. 9** The two meshes A (top) and B (bottom) used in the blood nozzle simulations.

The distributions of velocity magnitude in the nozzle after reaching steady state are shown in figure 10 and 11. It can be observed that the sudden expansion at the exit of the throat leads to the formation of a jet. In the turbulent regime, the center velocity of jet has a sudden decrease called jet breakdown. Most of the results show the breakdown of the jet, but with different breakdown locations. This can be shown clearly in figure 12 depicting the velocity along the center line of the nozzle, where the origin of the axial coordinate is at the exit of the throat (figure 8). It can be observed that the results by PFEM-2 have good agreement with experimental result by [7] with both meshes. Also, the results using PFEM-2 are not affected much by the time step size, since the convection terms are taken care of separately. However, for the results using FEM, it can be affected largely once CFL number is larger than 1. Also, the breakdown locations are also affected by the mesh

configuration. This may be due to the additional viscosity added through the convection stabilization term in this FEM algorithm. [NEEDS CHECKING]

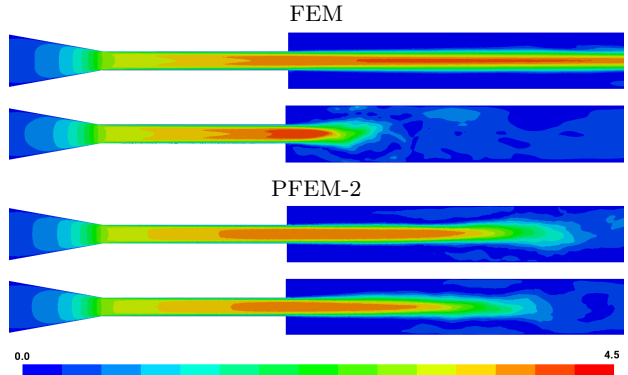


**Fig. 10** The magnitude of velocity field at steady state with mesh A using FEM and PFEM-2 with CFL number equals to 1 (1st and 3rd plots) and 5 (2nd and 4th plots).

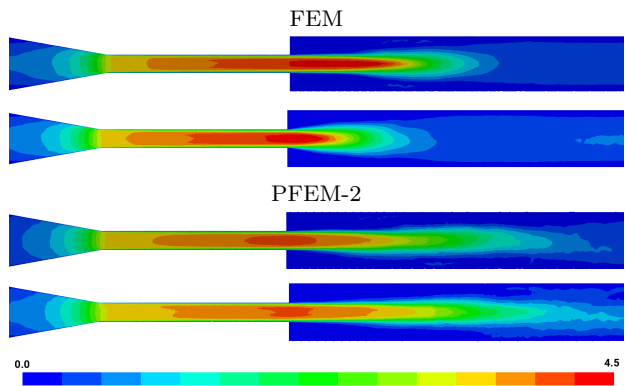


**Fig. 11** The magnitude of velocity field at steady state with mesh B using FEM and PFEM-2 with CFL number equals to 1 (1st and 3rd plots) and 10 (2nd and 4th plots).

#### 4.2 Blood Pump

The geometry of the simplified centrifugal pump is shown in the figure 13. The flow enters the chamber through a curved tube with diameter 12 mm. The diameter of the inner chamber of the housing is 60 mm and the thickness is 9 mm. The rotor inside the chamber is with diameter 52 mm and 4 mm thick, along with four 3 mm thick straight blades. The chamber is connected with a throat at its outlet, followed by a diffuser to the outlet tube with diameter 12 mm. The pump flow with flowrate  $Q = 6 \text{ L/min}$  and rotational speed 3500 RPM is simulated.

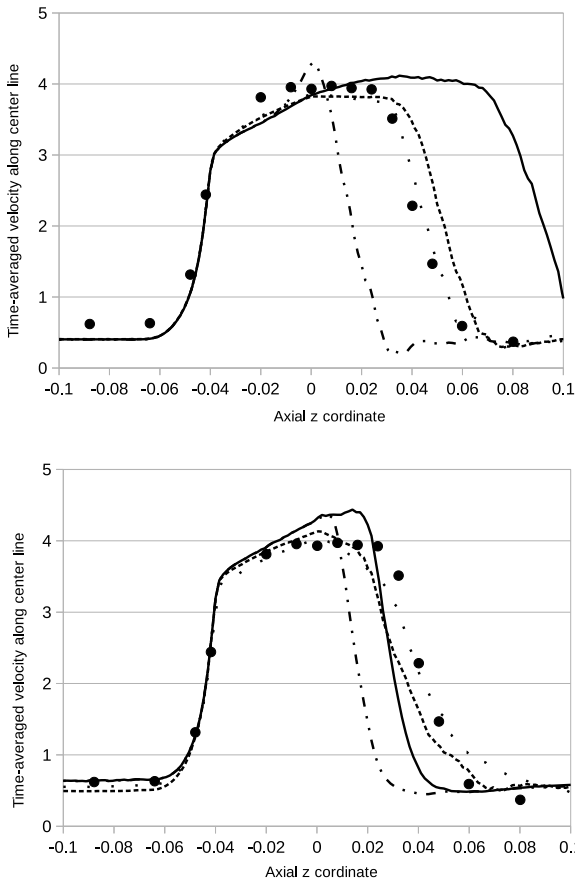


**Fig. 12** The distribution of the axial velocity in the nozzle along the center line. The top figure depicts the results with mesh A using FEM+CFL1 (solid), FEM+CFL5 (dash-dotted), PFEM-2+CFL1 (dashed) and PFEM2+CFL5 (dotted). The bottom figure depicts the results with mesh B using FEM+CFL1 (solid), FEM+CFL10 (dash-dotted), PFEM-2+CFL1 (dashed) and PFEM2+CFL10 (dotted).

As to the simulation set up, the velocity distribution is prescribed at the inlet (see figure 13 bottom plot), where the velocity profiles are obtained from the experimental measurements using PIV from [2]. The pressure at the outlet is set to be constant, and the gravitational force is included. Since the goal is to predict the flow field after it reaching steady state, instead of letting the rotor rotate during simulation, the non-inertial reference frame is applied on the fluid around the rotor. This is because the flow around the rotor at steady state can be analogue to flow experiencing constant angular velocity. Using non-inertial reference frame avoids mesh distortion and frequent remeshing due to rotation. For turbulence model, the LES Wall-Adapting Local Eddy-viscosity (WALE) model is employed, with 7% of turbulence intensity imposed at the inlet.

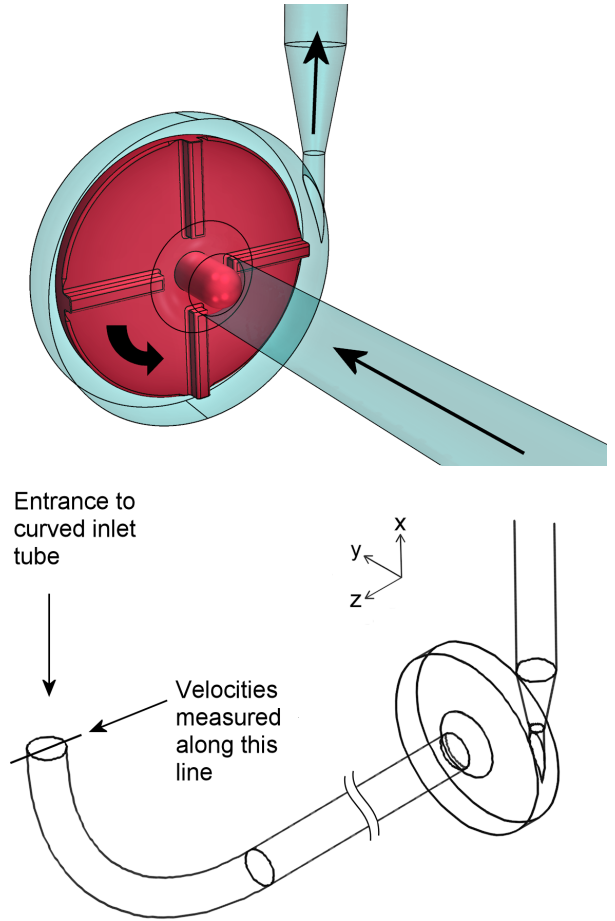


**Fig. 13** The geometry of and the flow direction in the blood pump (top), and the location where the velocity is measured in the experiments the velocity profile is prescribed in the simulations (right).

The simulation domain is decomposed into around 1 million tetrahedron elements. The mesh size is 0.5 mm on the rotor blades and 0.3 mm at the outlet of the chamber to diffuser. The mesh is locally refined around the throat as shown in figure 14. The simulation result is obtained after 15 rotations of the rotor, when the pump flow already reaches steady state. The time step size is around  $10^{-5}$  s in FEM and PFEM-2 simulations at steady state so that the CFL number is less or equal than 1.

The obtained pressure difference across the pump by experiment and simulations are listed in table 1. Using FEM the discrepancy with experiment is only 3.6%. On the other hand, PFEM-2 predicts a much higher pressure difference. From the distribution of the velocity and pressure fields in the chamber (figure 15 and 16, it can be observed that the velocity pattern obtained with PFEM-2 is different from FEM. With PFEM-2, the velocity is higher mainly in front of the leading edge

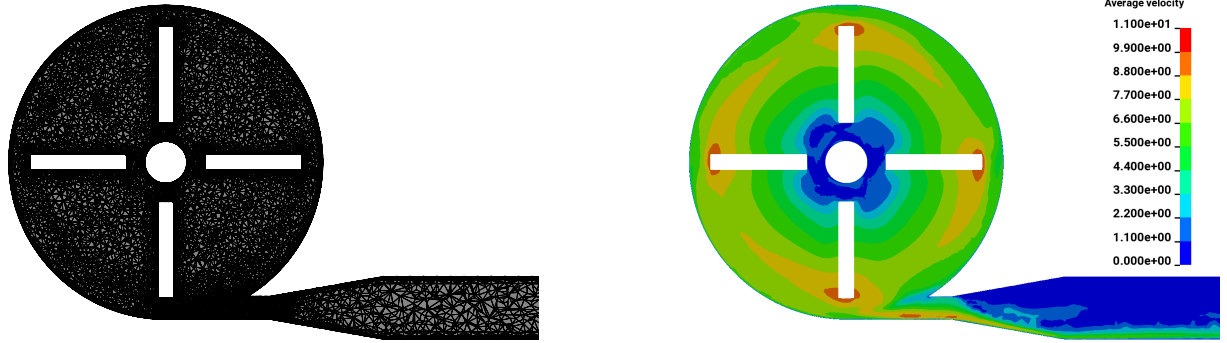


**Fig. 14** The mesh configuration used in the pump flow simulation on the plane which coincides to the mid-axis plane of the outlet diffuser.

of the blade, where with FEM, the velocity is higher at both side of the blade, but more near the trailing edge. \*\*\*This might due to the nature of the particle method that the influence of the inertia is emphasised. So the particles pushed by the blades has less tendency to turn in chamber. This leads to a larger pressure gradient in the radial direction to make the particle turn. [NEEDS CHECKING]

**Table 1** The pressure differences accross the pump.

	Pressure (mmHg)
Experiment [11]	272.38
FEM	282.40
PFEM-2	489.64

Figure 17 depicts the comparison of velocity profile in the pump chamber and diffuser compared with experimental measurements reported in [11]. The velocity between blades by FEM is in accordance with experiments, where the result by PFEM-2 exhibits a lower slope near the blade tip. Both FEM and PFEM-2 predict the detached jet in the outlet diffuser leaning more against the outer wall. The velocity magnitude appears to be larger pbu FEM. These phenomenon may be due to using non-inertial reference frame approximation, since similar velocity distribution can also be observed in most of other numerical results also using non-inertial reference frame [11].

#### 4.3 Inferior Vena Cava

In this study, the geometry of the IVC system consists of two iliac veins merging to one infrarenal IVC as shown in figure 18. This patient-averaged IVC geometry is proposed by [12] from the CT data of 10 patients. The flows enter from the two iliac veins and merge after

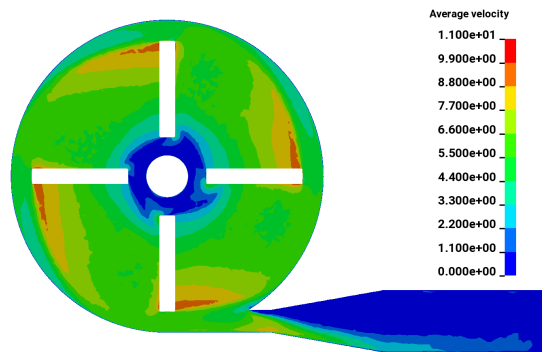


**Fig. 15** The magnitude of velocity distribution on the plane which coincides to the mid-axis plane of the outlet diffuser using FEM (top) and PFEM-2 (bottom).

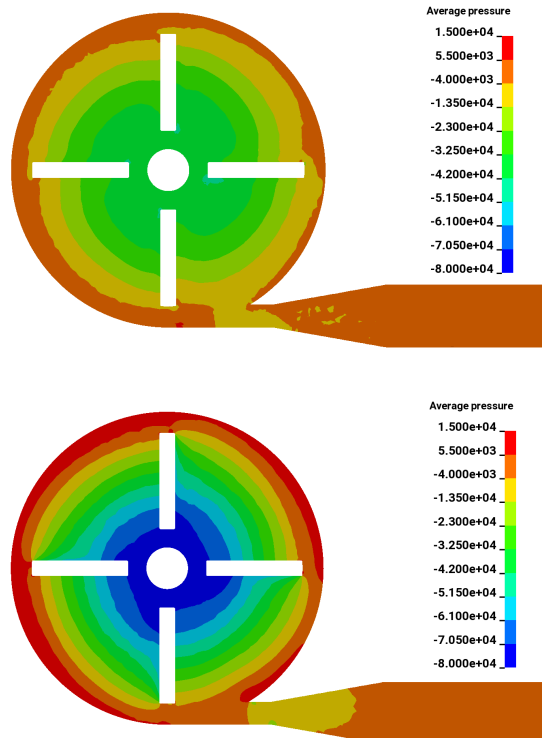


**Fig. 16** The pressure distribution on the plane which coincides to the mid-axis plane of the outlet diffuser using FEM (top) and PFEM-2 (bottom).

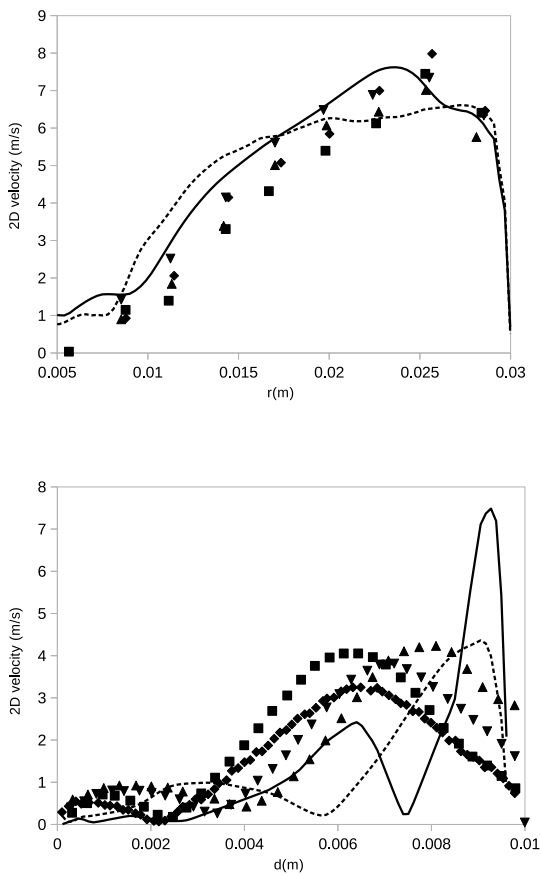


**Fig. 17** The magnitude of the two-dimensional velocity on the xy-plane passing the mid-axis plane of the outlet diffuser with experiments and simulations. Left: along the radial direction from the rotor center in the housing. Right: in the outlet diffuser.  $\blacktriangledown \blacktriangle \blacksquare \blacklozenge$ : experiments [11]. Solid line: FEM. Dashed line: PFEM-2.

entering the infrarenal IVC, which has hydraulic diameter about 28 mm. The simulations of the flow in IVC are conducted according to the parameters provided in [13]. The simulations of two flowrates are performed corresponding to the resting and exercising conditions, which are  $Q = 0.5$  (l/min) and 3 (l/min) into two iliac veins respectively. The corresponding Reynolds numbers for resting and exercising conditions are 236 and 1505. The flow is considered to be laminar in the IVC. For boundary conditions, the parabolic velocity profile is prescribed at the inlet of two iliac veins, and the constant pressure is imposed at the outlet of the infrarenal IVC. In the following section, a grid convergence study is performed on the IVC flow first using FEM at the exercising condition. Secondly, the simulation results using FEM and PFEM-2 will be compared with the PIV experimental results by [12].

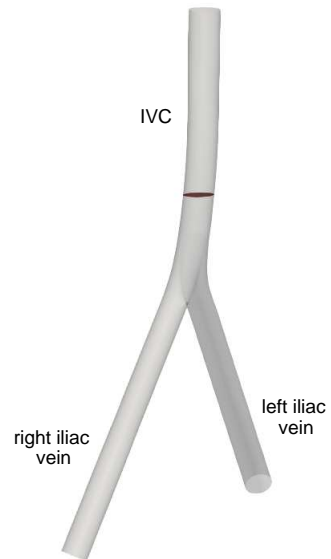


**Fig. 18** The patient-averaged IVC geometry proposed by [12].

#### Grid Convergence Test

In the grid convergence test, five kinds of tetrahedral mesh with different mesh sizes are used. The mesh sizes are from 0.45 mm to 2 mm so that the domain is decomposed into around 0.87 million to 37.94 million tetrahedra elements (table 2). The transverse cross-sections of mesh 2 and 4 located at around 10 cm downstream of the confluence of two iliac veins are shown in the figure 19.

**Table 2** Mesh used in the convergence test.

Mesh	Number of element ( $\times 10^6$ )	mesh size (mm)
1	0.87	2.0
2	2.04	1.4
3	4.70	1.0
4	17.68	0.6
5	37.94	0.45

The flow simulations with these five meshes are conducted using FEM at exercising condition. The simulation result will be evaluated not only qualitatively with the velocity magnitude field and local normalized helicity field on a transverse cross-sectional plane, but also quantitatively through three scalar quantities: maximum nodal velocity, area-averaged transverse velocity magnitude and volume-averaged helicity intensity. The helicity density  $h$ , which is defined as the inner product of vorticity and velocity  $h = u \cdot \omega$ , represents the tendency of the flow to have helical flow. The local nor-

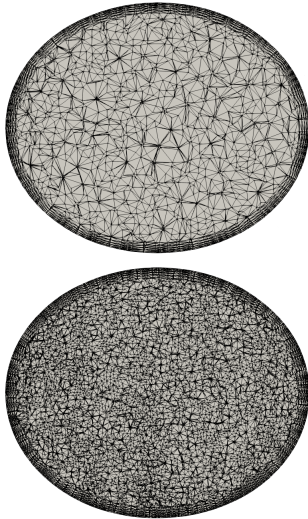


**Fig. 19** The transverse cross-sectional view of mesh number 2 (top) and number 4 (bottom) in the grid convergence study. The cross-section is located at around 10 cm downstream of the confluence of two iliac veins.

malized helicity (LNH) is

$$LNH = \frac{\mathbf{u} \cdot \boldsymbol{\omega}}{|\mathbf{u}| |\boldsymbol{\omega}|}, \quad (17)$$

and the volume-averaged helicity intensity  $\overline{HI}$  can be calculated using

$$\overline{HI} = \frac{1}{V} \int_V |\mathbf{u} \cdot \boldsymbol{\omega}| dV. \quad (18)$$

The area-averaged transverse velocity magnitude,

$$\overline{|u_{tr}|} = \frac{1}{A} \int_A |u_{\parallel}| dA, \quad (19)$$

where  $u_{\parallel}$  is the velocity component parallel to the surface, indicates the measure of the secondary flow. The velocity magnitude field, LNH, and  $\overline{|u_{tr}|}$  will be examined on the transverse cross-sectional plane located at 10 cm downstream of the confluence point in the present study.

The obtained velocity magnitude field and LNH field with above-mentioned five meshes on the same transverse cross-sectional plane are shown in figure 20 and 21. It can be observed that the resulting flow velocity fields with different sizes of meshes have the similar patterns, but the some flow details are unresolved with mesh 1 and 2. This phenomenon can also be seen in the resulting LNH fields.

The quantitative analysis of the convergence study using maximum nodal velocity, area-averaged transverse velocity magnitude and volume-averaged helicity intensity are tabulated in table 3, where  $p$  represent the order of convergence [ADD REFERENCE]. It can be observed that the transverse velocity and helicity values

converge when meshes get finer. But for the maximum nodal velocity, the trend is monotonic except for the result by mesh 1. This might be because the nodal maximum velocity is still affected by how the domain is decomposed. In the following section, the mesh 2 and 3 will be utilized in the simulation of IVC flows at resting and exercising conditions.

### Comparison with Experimental Results

The velocity fields predicted by FEM and PFEM-2 solvers will be compared quantitatively with PIV experimental result by [12] on a selected sagittal plane and a coronal plane indicated at two flow conditions in figure 22. The FEM and PFEM-2 solvers use the same mesh under the same flow condition. The experimental and simulation results of the in-plane 2D velocity magnitudes in the sagittal and coronal planes at resting and exercising conditions are shown in the figure 23 and 24. It shows that the results by FEM and PFEM-2 solvers both match qualitatively with the PIV results.

To do quantitative comparison with experiments, the numerically obtained nodal velocities are firstly sampled on to the PIV data points. The magnitude of 2D plane velocity is then calculated on each data points. The global relative error,  $E$ , can be obtained by averaging the relative error between numerical and experimental result on all the points. Table 4 and 5 shows the global relative error at different flow conditions with FEM, PFEM-2 solvers as well as the numerical analysis reported in [13]. The global relative error is around 5 to 6% at resting condition and 6 to 11% at exercising condition. The numerical results have a good agreement with the experimental data. For both conditions, the FEM and PFEM-2 results have similar amount of global relative error with [13]. It is worth noting that the mesh sizes used here (1.4 mm for resting and 1 mm for exercising) are coarser than the mesh size (0.276 mm) used in [13]. Also, the PFEM-2 has nearly the same error with FEM at resting condition, and even less error in the coronal plane at exercising condition.

## 5 Conclusions

### References

1. FDA's "Critical Path" Computational Fluid Dynamics (CFD)/Blood Damage Project: Computational Round Robin problems [https://nciphub.org/wiki/FDA\\_CFD](https://nciphub.org/wiki/FDA_CFD)
2. FDA Critical Path Initiative (CPI) <https://www.fda.gov/science-research/special-topics/critical-path-initiative/default.htm>
3. Hariharan, P., Giarra, M., Reddy, V., Day, S.W., Manning, K.B., Deutscher, S., Stewart, S.F., Myers, M.R., Berman,

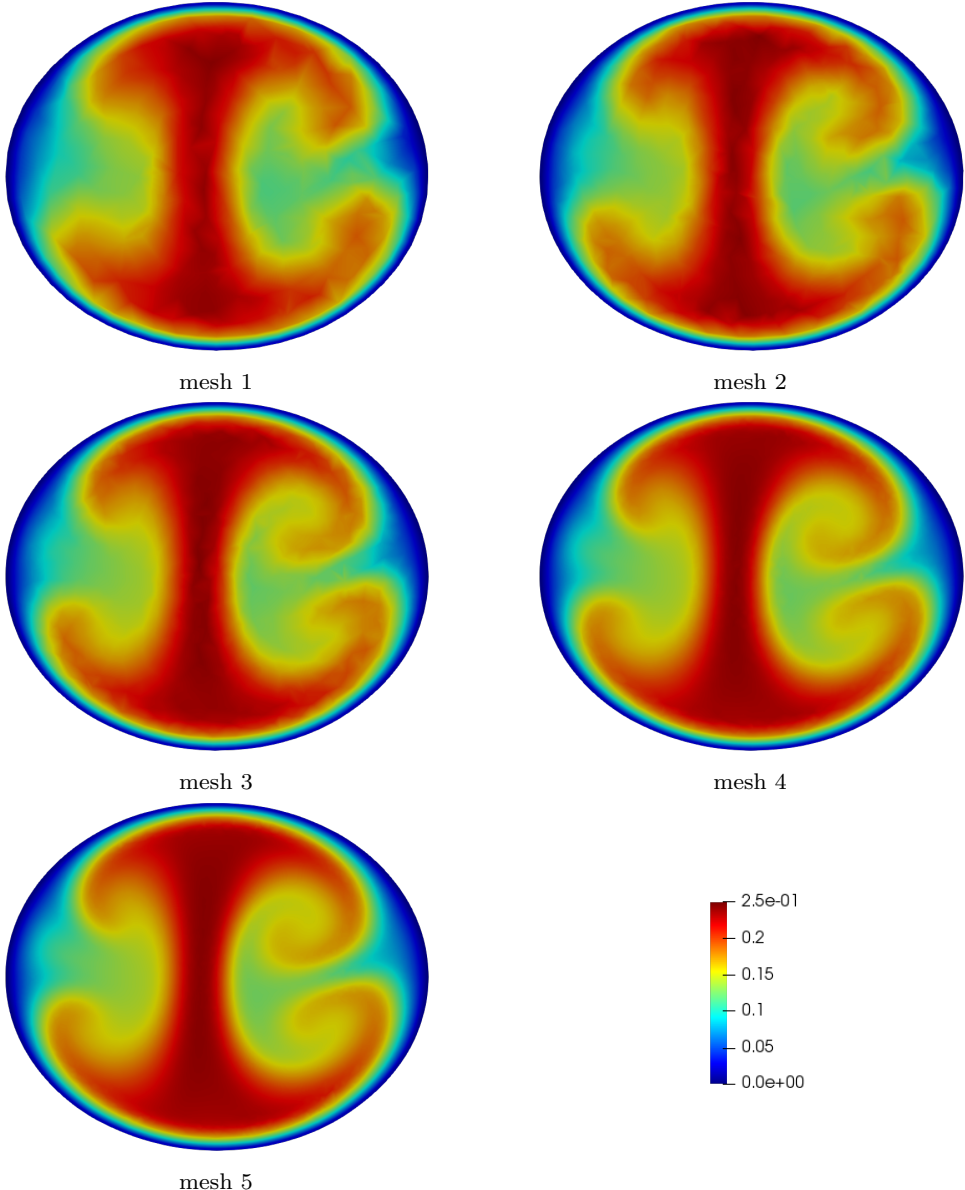


**Fig. 20** The velocity magnitude fields using different sizes of mesh.

- M.R., Burgreen, G.W. and Paterson, E.G. (2011). Multi-laboratory particle image velocimetry analysis of the FDA benchmark nozzle model to support validation of computational fluid dynamics simulations. *Journal of Biomechanical Engineering*, 133(4), 041002.
4. Herbertson, L. H., Olia, S. E., Daly, A., Noatch, C. P., Smith, W. A., Kameneva, M. V., & Malinauskas, R. A. (2015). Multilaboratory Study of Flow-Induced Hemolysis Using the FDA Benchmark Nozzle Model. *Artificial organs*, 39(3), 237-248.
  5. Giarra, M. N. (2009). Shear Stress Distribution and Hemolysis Measurements in a Centrifugal Blood Pump. Rochester Institute of Technology.
  6. Zmijanovic, V., Mendez, S., Moureau, V., & Nicoud, F. (2017). About the numerical robustness of biomedical benchmark cases: Interlaboratory FDA's idealized medical device. *International journal for numerical methods in biomedical engineering*, 33(1).
  7. Hariharan, P., D'Souza, G. A., Horner, M., Morrison, T. M., Malinauskas, R. A., & Myers, M. R. (2017). Use of the FDA nozzle model to illustrate validation techniques in computational fluid dynamics (CFD) simulations. *PloS one*, 12(6), e0178749.
  8. Nassau, C. J., Wray, T. J., & Agarwal, R. K. (2015, July). Computational Fluid Dynamic Analysis of a Blood Pump: An FDA Critical Path Initiative. In *ASME/JSME/KSME 2015 Joint Fluids Engineering Conference* (pp. V002T26A002-V002T26A002). American Society of Mechanical Engineers.
  9. Heck, M. L., Yen, A., Snyder, T. A., O'Rear, E. A., & Papavassiliou, D. V. (2017). Flow-Field Simulations and Hemolysis Estimates for the Food and Drug Administration Critical Path Initiative Centrifugal Blood Pump. *Artificial organs*, 41(10).
  10. Stewart, S. F., Paterson, E. G., Burgreen, G. W., Hariharan, P., Giarra, M., Reddy, V., Stewart, S.F., Paterson,

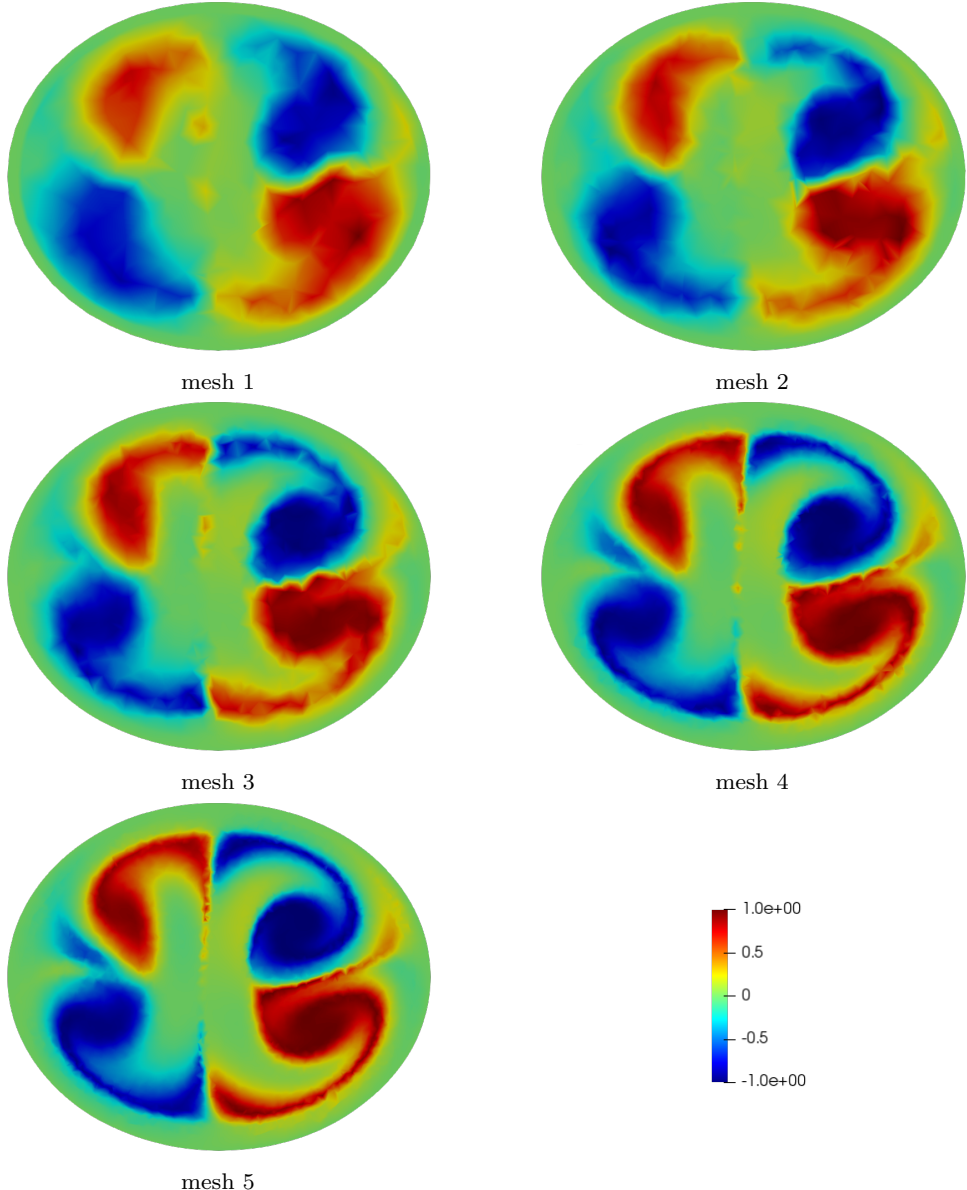


**Fig. 21** The local normalized helicity (LNH) fields.

**Table 3** The value of maximum velocity, transverse velocity, Helicity and the corresponding order of convergence  $p$ .

Mesh	maximum velocity		transverse velocity		Helicity	
	$ u _{max}$	$p$	$ u_{tr} $	$p$	$\bar{HI}$	$p$
1	0.2549		0.0238		0.3807	
2	0.2585		0.0244		0.4132	
3	0.2567	2.36	0.0247	2.40	0.4331	1.63
4	0.2541	0.31	0.02497	2.24	0.4498	1.84
5	0.2534	2.16	0.02502	2.88	0.4536	2.54

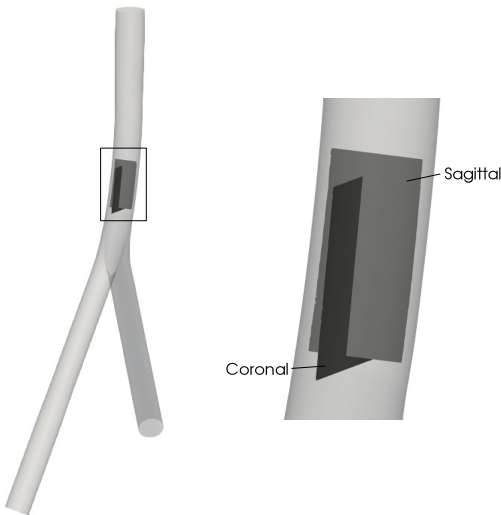


**Fig. 22** The sagittal and coronal planes where the velocity field are measured in experiments ([12]).

**Table 4** Global relative error (%) between CFD and PIV at resting condition.

	Coronal	Sagittal
[13]	3.07	6.77
FEM	4.83	6.62
PFEM-2	4.79	6.65

**Table 5** Global relative error (%) between CFD and PIV at exercising condition.

	Coronal	Sagittal
[13]	10.98	5.56
FEM	11.28	5.93
PFEM-2	10.44	6.10

- E.G., Burgreen, G.W., Hariharan, P., Giarra, M., Reddy, V., Day, S.W., Manning, K.B., Deutsch, S., Berman, M.R. and Myers, M.R. (2012). Assessment of CFD performance in simulations of an idealized medical device: results of FDA's first computational interlaboratory study. *Cardiovascular Engineering and Technology*, 3(2), 139-160.
11. Malinauskas, R. A., Hariharan, P., Day, S. W., Herbertson, L. H., Buesen, M., Steinseifer, U., Aycock, K.I., Good, B.C., Deutsch, S., Manning, K.B. and Craven, B.A. (2017). FDA benchmark medical device flow models for CFD validation. *ASAIO Journal*, 63(2), 150-160.
  12. Gallagher, M. B., Aycock, K. I., Craven, B. A., & Manning, K. B. (2018). Steady flow in a patient-averaged inferior vena cava—part I: particle image velocimetry measurements at rest and exercise conditions. *Cardiovascular engineering and technology*, 9(4), 641-653.
  13. Craven, B. A., Aycock, K. I., & Manning, K. B. (2018). Steady Flow in a Patient-Averaged Inferior Vena Cava—Part II: Computational Fluid Dynamics Verification and Validation. *Cardiovascular engineering and technology*, 9(4), 654-673.
  14. Monaghan JJ (1988) An introduction to SPH. *Comput Phys Com- mun* 48:89–96

15. Harlow FH (1955) A machine calculation method for hydro- dynamic problems. Los Alamos Scientific Laboratory Report LAMS-1956
16. Harlow FH, Welch J (1965) Numerical calculation of time dependent viscous incompressible flow of fluid with free surface. *Phys Fluids* 8(12):2182–2189
17. Wieckowsky Z (2004) The material point method in large strain engineering problems. *Comput Methods Appl Mech Eng* 193(39):4417–4438
18. S. Koshizuka and Y. Oka, "Moving particle semi-implicit method for fragmentation of incompressible fluid," Nuclear Science and Engineering, Vol 123, pp. 421–434, 1996.
19. Idelsohn SR, Oñate E, Del Pin F (2004) The particle finite element method a powerful tool to solve incompressible flows with free- surfaces and breaking waves. *Int J Numer Methods* 61:964–989
20. Idelsohn SR, Nigro NM, Limache A, Oñate E (2012) Large time-step explicit integration method for solving problems with dominant convection. *Comput Methods Appl Mech Eng* 217– 220:168–185
21. Idelsohn SR, Nigro NM, Gimenez JM, Rossi R, Martí J (2013) A fast and accurate method to solve the incompressible Navier– Stokes equations. *Eng Comput* 30(2):197–222
22. Gimenez JM, Nigro NM, Idelsohn SR (2014) Evaluating the performance of the particle finite element method in parallel architectures. *J Comput Part Mech* 1(1):103–116
23. Hestenes, Magnus R.; Stiefel, Eduard (December 1952). Methods of Conjugate Gradients for Solving Linear Systems. *Journal of Research of the National Bureau of Standards*. 49 (6). doi:10.6028/jres.049.044.
24. Idelsohn SR, Martí J, Becker P, Oñate E (2014) Analysis of multi-fluid flows with large time steps using the particle finite element method. *Int J Numer Methods Fluids* 75(9):621–644
25. Gimenez JM, Gonzlez LM (2015) An extended validation of the last generation of particle finite element method for free surface flows. *J Comput Phys* 284:186–205
26. Becker P, Idelsohn SR, Oñate E (2014) A unified monolithic approach for multi-fluid flows and fluid-structure interaction using the particle finite element method with fixed mesh. *Comput Mech* 55(6):1091–1104
27. Gimenez JM, Nigro N, Oñate E, Idelsohn S (2016) Surface tension problems solved with the particle finite element method using large time-steps. *Comput Fluids*
28. Gimenez JM (2015) Enlarging time-steps for solving one and two phase flows using the particle finite element method. Ph.D. Thesis, Universidad Nacional del Litoral, Santa Fe, Argentina
29. Ramon Codina, Orlando Soto, Approximation of the incompressible Navier–Stokes equations using orthogonal subscale stabilization and pressure segregation on anisotropic finite element meshes, *Computer Methods in Applied Mechanics and Engineering*, Volume 193, Issues 15–16, 2004, Pages 1403-1419, ISSN 0045-7825, <https://doi.org/10.1016/j.cma.2003.12.030>.
30. Ramon Codina, Stabilization of incompressibility and convection through orthogonal sub-scales in finite element methods, *Computer Methods in Applied Mechanics and Engineering*, Volume 190, Issues 13–14, 2000, Pages 1579–1599, ISSN 0045-7825, [https://doi.org/10.1016/S0045-7825\(00\)00254-1](https://doi.org/10.1016/S0045-7825(00)00254-1).
31. A.J. Chorin, *Math. Comput.* 22,745 (1968)
32. R. Temam, *Arch. Rat. Mech. Anal.* 32, 377 (1969)
33. J. Gimenez, Enlarging time steps for solving one and two phase flows using the particle finite element method, Ph.D. thesis, Facultad de Ingeniería y Ciencias Hídricas - Centro

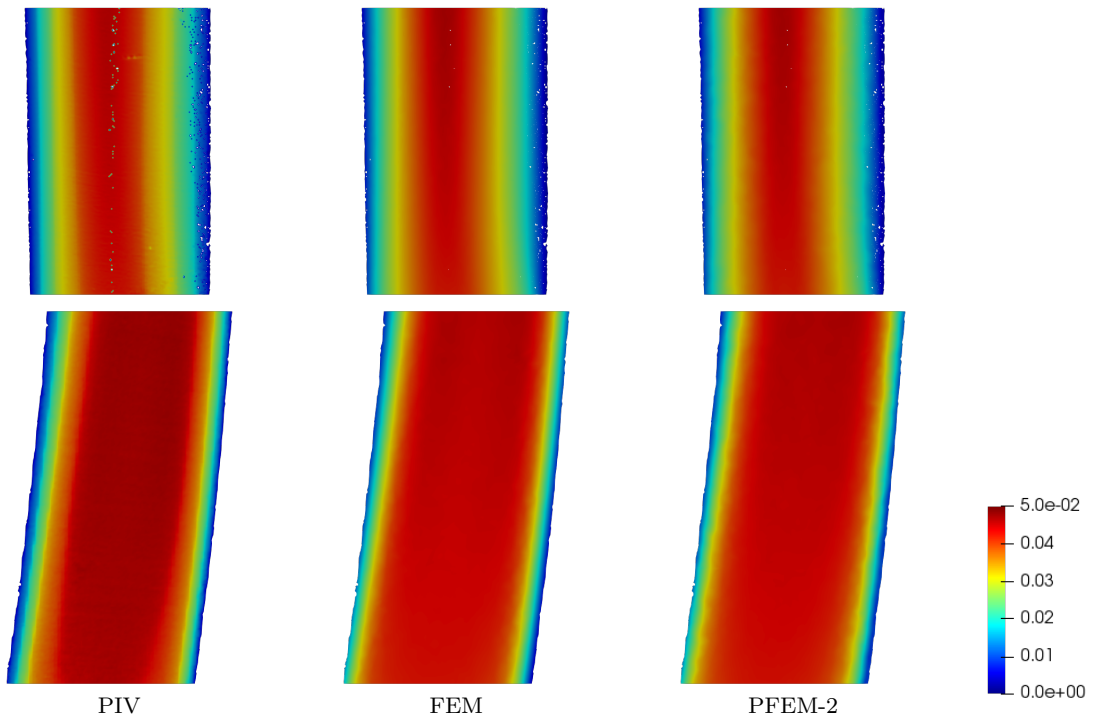


**Fig. 23** The in-plane 2D velocity magnitude in coronal (top) and sagittal (bottom) planes of PIV, FEM and PFEM-2 results at resting condition

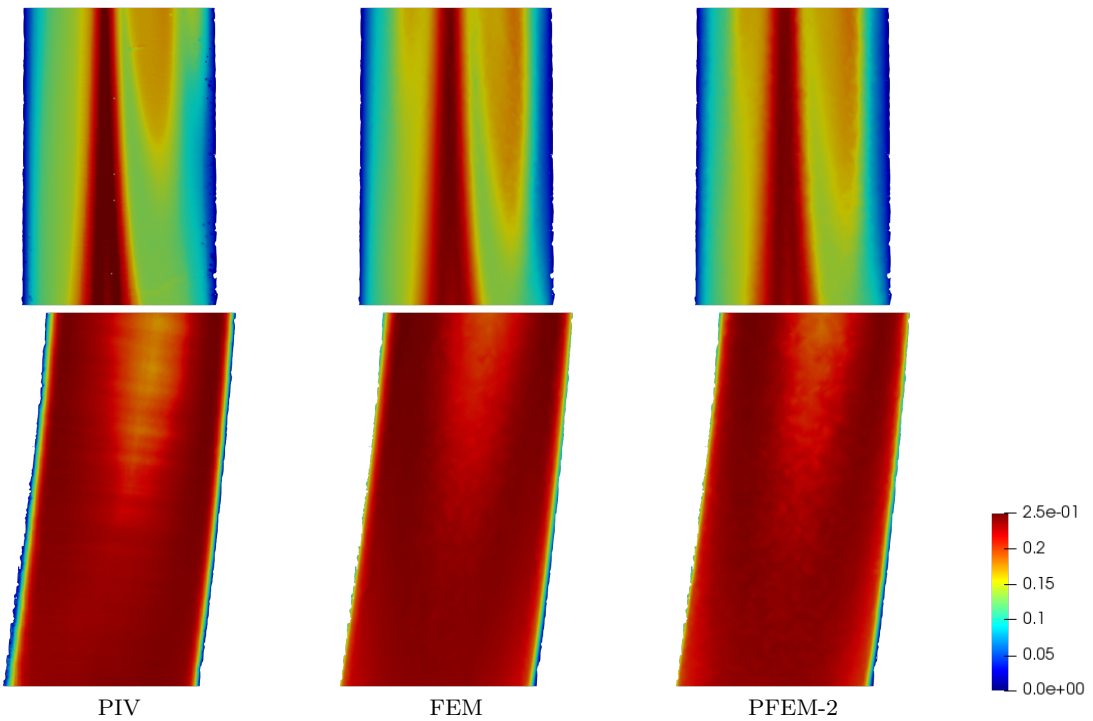


**Fig. 24** The in-plane 2D velocity magnitude in coronal (top) and sagittal (bottom) planes of PIV, FEM and PFEM-2 results at resting condition

- de Investigaciones en Mecanica Computacional. Santa Fe, Argentina (2015).
- 34. George Karypis, Vipin Kumar, METIS, a Software Package for Partitioning Unstructured Graphs and Computing Fill-Reduced Orderings of Sparse Matrices
  - 35. George Karypis, Vipin Kumar, A fast and high quality multilevel scheme for partitioning irregular graphs, SIAM Journal on Scientific Computing, Volume 20, Number 1, 1998, pages 359-392;
  - 36. Gimenez JM, Nigro NM, Idelsohn SR (2012) Improvements to solve diffusion-dominant problems with PFEM-2. Mecanica Comput XXXI:137–155